

First Chromospheric Activity and Doppler Imaging Study of PW And Using a New Doppler Imaging Code: SpotDIPy

ENGIN BAHAR,¹ HAKAN V. ŞENAVCI,¹ EMRE IŞIK,^{2,3} GAITEE A.J. HUSSAIN,⁴ OLEG KOCHUKHOV,⁵ DAVID MONTES,⁶ AND YUE XIANG^{7,8}

¹*Department of Astronomy and Space Sciences, Faculty of Science, Ankara University, Beşevler 06100, Ankara, Türkiye*

²*Max-Planck-Institut für Sonnensystemforschung, Justus-von-Liebig-Weg 3, 37077 Göttingen, Germany*

³*Department of Computer Science, Turkish-German University, Beykoz 34820, Istanbul, Türkiye*

⁴*European Space Agency (ESA), European Space Research and Technology Centre (ESTEC), Keplerlaan 1, 2201 AZ Noordwijk, The Netherlands*

⁵*Department of Physics and Astronomy, Uppsala University, Box 516, SE-75120 Uppsala, Sweden*

⁶*Departamento de Física de la Tierra y Astrofísica & IPARCOS-UCM (Instituto de Física de Partículas y del Cosmos de la UCM), Facultad de Ciencias Físicas, Universidad Complutense de Madrid, E-28040 Madrid, Spain*

⁷*Yunnan Observatories, Chinese Academy of Sciences, Kunming 650216, People's Republic of China*

⁸*Key Laboratory for the Structure and Evolution of Celestial Objects, Chinese Academy of Sciences, Kunming 650216, People's Republic of China*

(Received MMM D, YYYY; Revised MMM D, YYYY; Accepted MMM D, YYYY)

Submitted to ApJ

ABSTRACT

Measuring coverage of dark spots on cool stars is important in understanding how stellar magnetic activity scales with the rotation rate and convection zone depth. In this respect, it is crucial to infer surface magnetic patterns on G and K stars, to reveal solar-like stellar dynamos in action. Molecular bands serve as invaluable indicators of cool spots on the surfaces of stars, as they play a crucial role in enabling accurate assessments of the extent of spot coverage across the stellar surface. Therefore, more reliable surface images can be obtained considering the inversion of atomic lines with molecular bands. In this context, we simultaneously carry out Doppler imaging (DI) using atomic lines as well as Titanium Oxide (TiO) band profiles of PW And (K2 V) and also investigate chromospheric activity indicators for the first time in the literature, using the high-resolution spectra. The surface spot distribution obtained from the inversion process represents both atomic line and TiO-band profiles quite accurately. The chromospheric emission is also correlated with photospheric spot coverage, except during a possible flare event during the observations. We detect frequent flare activity, using TESS photometry. We also introduce a new open-source, Python-based DI code SpotDIPy that allows performing surface reconstructions of single stars using the maximum entropy method. We test the code by comparing surface reconstruction simulations with the extensively used DoTS code. We show that the surface brightness distribution maps reconstructed via both codes using the same simulated data are consistent with each other.

Keywords: stars: activity, stars: imaging – starspots

1. INTRODUCTION

PW And is a rapidly rotating pre-main-sequence K2 V-type star, which is a member of the AB Doradus moving group. Its high Li I abundance also confirms

its membership to the young Local Association (Montes et al. 2001b,a; López-Santiago et al. 2003; Montes et al. 2004). Its projected rotational velocity, $v \sin i$, was determined by several investigators in the literature in the range from 21.5 km s⁻¹ (Griffin 1992) to 23.9 km s⁻¹ (Strassmeier & Rice 2006). A detailed activity investigation of PW And was performed by López-Santiago et al. (2003), who analysed photospheric Ca I and Fe I

line profiles using CCF bisector analysis (see [Dempsey et al. 1992](#), for more details) and found that the CCF bisectors change with a period similar to the photometric period of PW And, suggesting the presence of cool spots. Using the spectral subtraction technique ([Montes et al. 2000](#)), they also measured the equivalent width variation of chromospheric activity indicator lines from Ca II H&K to Ca II IRT lines along with the rotational phase and found that the chromospheric regions appear to be associated with the photospheric features obtained using CCF bisector analysis. In addition, they detected two flares in 2001 and 2002, confirming the strong magnetic activity of the star. [López-Santiago et al. \(2010\)](#) and [Lehtinen et al. \(2016\)](#) determined emission index as $\log R'_{HK}$ -3.85 and -4.217, respectively, revealing the highly active chromosphere. The first DI of PW And was obtained by [Strassmeier & Rice \(2006\)](#), using high-resolution CFHT spectroscopy. They found that cool spots are located within an equatorial band up to $\pm 40^\circ$ of the stellar equator, with temperature contrast relative to the immaculate photosphere of up to $\Delta T = 1200$ K. They also estimated a set of astrophysical parameters (see Table 1 of [Strassmeier & Rice 2006](#), for more details), including the rotation period as 1.76159 days, using high-precision photometry. Another DI analysis was carried out by [Gu et al. \(2010\)](#), who used high-resolution spectra obtained at the Xinglong Station of National Astronomical Observatories (NAOC) and Bohyunsan Astronomical Observatory (BOAO). Their spectra were separated into two subsets spanning approximately one month. Unlike the Doppler images presented by [Strassmeier & Rice \(2006\)](#), their resulting spot distributions were rather concentrated within intermediate to high latitudes, while weaker low-latitude spots were also visible. They also reported that there is no notable position variation of spots and concluded that intermediate- to high-latitude spots have lifetimes longer than a month. Based on the high-resolution spectroscopic observations carried out at the RTT-150 telescope of TÜBİTAK National Observatory, the most recent DI was performed by [Kolbin & Galeev \(2017\)](#). They found that spots were located around latitude 40° and claimed that the resultant map is similar to that obtained by [Strassmeier & Rice \(2006\)](#), where spots spread between 0° - 40° with a tendency toward 30° .

The latitudinal distributions of spots on PW And that were inferred in previous studies are substantially different from each other. Possible underlying reasons are the image reconstruction process and intrinsic variations of spot distribution on the star between different epochs. New observations carried out at different epochs are thus needed to improve the basic statistics of the latitudinal

spot distribution. Another reason for reexamining PW And, apart from previous DI studies based on atomic lines, is to simultaneously confirm the spot distribution and contrast using TiO-band at 7055 \AA in this research.

In this study, we conducted a simultaneous analysis of both atomic line and TiO-band profiles with the DI technique on PW And, using three distinct sets of observations spanning different time intervals. Concurrently, we investigated chromospheric activity within the same dataset and compared the observed activity trends. Additionally, an accurate rotation period of PW And was calculated using the Lomb-Scargle periodogram and $v \sin i$ was determined on a 2D grid search. We also introduced a new open-source and user friendly Python-based DI code `SpotDIPy` and tested via `DoTS` ([Collier Cameron 1992](#)).

2. OBSERVATIONS AND DATA REDUCTION

We obtained a high-resolution spectral time-series of PW And, using the HERMES¹ spectrograph ([Raskin et al. 2011](#)) attached to the 1.2-m Mercator telescope at the Roque de los Muchachos Observatory (La Palma, Spain), between 14-19 December in 2015 (hereafter Set-1), 25-29 September in 2018 (hereafter Set-2) and 14-19 December in 2018 (hereafter Set-3). Consequently, Set-1, Set-2 and Set-3 data of PW And obtained in this study cover approximately 2.9, 2.4 and 2.3 rotational cycles, respectively.

The average spectral resolution is $R=85\,000$ with a wavelength coverage between 3780 and 9007 \AA . The data were acquired using exposure times between 1200 and 1800 seconds, which yielded signal-to-noise ratios (S/N) between 73 and 174. The S/N values of the spectra are given as per pixel around 550 nm. The effective spectral resolution is between 0.045-0.106 \AA in wavelength and 3.5 km/s in velocity units, while the sampling is 2 pixels per resolution element. The log of HERMES observing run is given in Table 1. The reduction of the spectra were performed using the automatic pipeline of the spectrograph ([Raskin et al. 2011](#)). The pipeline was utilized to execute fundamental echelle data reduction procedures, encompassing tasks such as bias, flat-field and the inter-order background level corrections, as well as the extraction of 1D spectra and subsequent wavelength calibration. The normalization procedure was carried out via a Python code developed by our working group ([Şenavcı et al. 2018](#)).

¹ Based on observations obtained with the HERMES spectrograph mounted on the 1.2 m Mercator Telescope at the Spanish Observatorio del Roque de los Muchachos of the Instituto de Astrofísica de Canarias.

We used the multi-line technique, Least Squares Deconvolution (hereafter LSD) (Donati et al. 1997), to produce a mean photospheric line profile with higher S/N, in turn improving the quality of the resulting spot maps. The line mask, contains information on the line positions and relative strengths, and is required to construct the mask used by LSD. We extracted the line mask from the Vienna Atomic Line Database (VALD) (Kupka et al. 1999). The wavelength regions including lines that are affected by chromospheric heating (i.e. Hydrogen Balmer series, Na I (D₁, D₂), Ca II IRT) and strong telluric lines were removed from the list to prevent any artifacts in the LSD profiles. We set the velocity increment to 1.75 km s⁻¹, considering spectral resolution (3.5 km s⁻¹) and its sampling (2) in pixel. We obtained LSD profiles of PW And with S/N in the range between 670 and 850. An example of a part of an input spectrum and the resultant LSD profile are shown in Figure 1.

The Transiting Exoplanet Survey Satellite (Ricker et al. 2015, TESS) photometry of PW And enabled us to determine the rotation period with high precision. TESS observed PW And in sectors 17 and 57, corresponding to time spans of October 8 - November 2, 2019 and September 30 - October 29, 2022, respectively. All of the light curve data presented in this paper were obtained from the Mikulski Archive for Space Telescopes (MAST²) at the Space Telescope Science Institute. The specific observations analyzed can be accessed via DOI. Among the two types of photometric data available, SAP flux is generated by summing all pixel values in a pre-defined aperture as a function of time, while PDCSAP flux is SAP flux from which long term trends have been removed, using so-called Co-trending Basis Vectors (CBVs). Since there is no amplitude difference between SAP and PDCSAP light curve data, we used the latter one to determine the rotation period of PW And.

3. ANALYSIS

3.1. Rotation Period Estimation

Although the TESS sectors 17 and 57 are about three years apart, the light curve morphology remains almost the same in both sectors as a dominant sinusoidal variation. This is shown in Figure 2 (upper panels). To investigate periodicities owing to the rotational modulation by spots, we computed the Lomb-Scargle periodogram, using the light curves from both sectors, after removing outliers and flares. The periodogram shows a clear peak (Figure 2, lower left panel), correspond-

Table 1. Phase-ordered spectroscopic observation log of PW And.

Date	Exp. Time (sec.)	BJD _{Mid}	Phase _{Mid}	S/N
18.12.2015	1800	57375.45063	0.002	108
15.12.2015	1200	57372.32557	0.223	74
19.12.2015	1800	57376.30420	0.488	77
19.12.2015	1800	57376.32584	0.500	73
19.12.2015	1800	57376.47665	0.586	104
14.12.2015	1600	57371.33483	0.659	92
16.12.2015	1800	57373.31890	0.788	102
18.12.2015	1800	57375.30685	0.920	108
25.09.2018	1500	58387.36672	0.066	155
25.09.2018	1500	58387.45742	0.117	172
27.09.2018	1500	58389.40298	0.225	119
27.09.2018	1500	58389.47599	0.266	142
29.09.2018	1500	58391.39726	0.360	170
29.09.2018	1500	58391.50205	0.420	174
26.09.2018	1500	58388.40970	0.659	169
27.09.2018	1500	58388.51470	0.719	169
15.12.2018	1600	58468.35045	0.168	79
17.12.2018	1600	58470.31374	0.286	154
17.12.2018	1600	58470.43395	0.354	161
18.12.2018	1200	58470.51817	0.402	135
14.12.2018	1600	58467.44046	0.650	105
16.12.2018	1600	58469.35515	0.740	111
16.12.2018	1600	58469.46048	0.800	126
18.12.2018	1200	58471.31222	0.854	140
18.12.2018	1200	58471.43170	0.922	144
19.12.2018	1200	58471.51305	0.968	129

ing to 0.569280 *days*⁻¹ in the frequency domain and 1.756604 ± 0.000015 days in the period domain. The period and its associated uncertainty were determined by fitting the peak using a Gaussian function through the least-squares method, along with the application of the bootstrap method. The resultant period is close to 1.76159 days obtained by Strassmeier & Rice (2006). The phase-folded light curves in Figure 2 show that the Sector 17 data has a higher amplitude compared to Sector 57, while both sector data show similar modulations. All the photometric and spectroscopic data used in analysis are phased using the following equation:

$$\text{BJD} = 2453200.00 + 1^{\text{d}}.756604 \times E. \quad (1)$$

3.2. Stellar Parameters Estimation

We obtained the stellar parameters of PW And using the spectral synthesis fitting method. Synthetic spectra were produced using the SPECTRUM (Gray & Cor-

² <https://mast.stsci.edu>

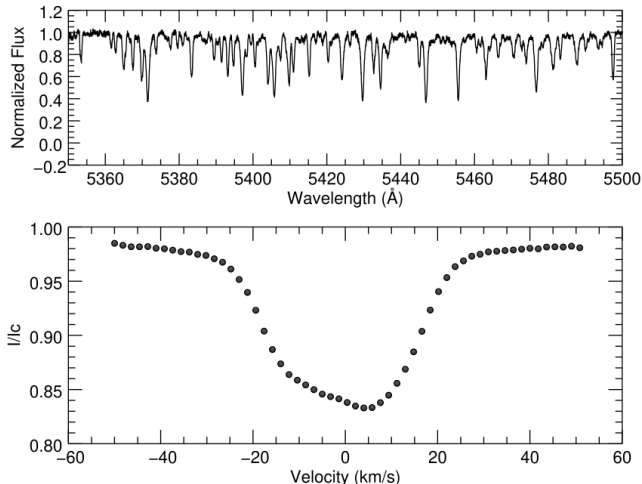


Figure 1. The input spectrum (top panel) and the resultant LSD profile (bottom panel) of PW And, corresponding to the rotational phase 0.002 of Set-1. Note that only a part of the input spectrum is shown here for better visualization.

bally 1994) code with MARCS (Gustafsson et al. 2008) atmosphere models and the VALD line list. The fitting was performed on all Fe I and Fe II lines in the wavelength range of 5400 - 6800 Å of the stellar spectrum. This region was selected because it contains relatively few telluric lines and the continuum can be more easily detected. All of these operations were carried out through iSpec (Blanco-Cuaresma et al. 2014; Blanco-Cuaresma 2019). The obtained parameters and errors were calculated using the bootstrap method. The resultant parameters are given in Table 2, which is consistent with the parameters obtained by Folsom et al. (2016), recently. A comparison of the synthetic spectrum and the observed spectrum is shown in Figure 3.

3.3. Doppler Imaging Code: SpotDIPy

To reconstruct the distribution of starspots, we developed a DI code, SpotDIPy, written in Python programming language. The code generates synthetic line profiles (R_{calc}) by integrating local line profiles across the entire visible stellar surface at each rotational phase, ϕ . Each surface element on the stellar surface consist of two line profiles with different temperatures, one representing the photosphere and the other representing the spots. This is a basic assumption for the DI method based on the two-temperature model with the resulting distribution in terms of spot filling factors, f_s , defined as the fraction of the surface element area occupied by spots. During the integration process, local line profiles are shifted and scaled with respect to the position of the surface element in the velocity space and the projected areas, respectively. The local line profiles also are scaled

with continuum flux ratio calculated from blackbody assumption based on their corresponding temperatures and central wavelengths. Limb- and gravity-darkening effects are taken into account during reconstruction. Limb-darkening coefficients are calculated by a Python package, ExoTiC-LD (Grant & Wakeford 2022). The intensity factors due to the gravity-darkening effect are determined, considering the study by Espinosa Lara & Rieutord (2011). SpotDIPy has two surface-grid mode, triangulation (supplied from PHOEBE2¹ Python package (Prša et al. 2016)) and trapezoidal discretization based on trapezoidal elements.

SpotDIPy uses the Maximum Entropy Method (MEM) to solve the ill-posed inverse problem, by taking a regularization function of the form

$$S(f_s) = - \sum_{i=1}^n w_i \left[f_{s_i} \log \frac{f_{s_i}}{m} + (1 - f_{s_i}) \log \frac{(1 - f_{s_i})}{(1 - m)} \right], \quad (2)$$

where w_i is the area of the i^{th} surface element and m is the default minimum fraction of spot coverage that is set to a very small, positive value. To find the best-fitting spot distribution over the visible part of the stellar surface, we use the error function

$$E = \sum_{\phi} \sum_{\nu} \left[\frac{R_{calc}(\nu, \phi) - R_{obs}(\nu, \phi)}{\sigma_{\nu, \phi}} \right]^2 + \lambda S, \quad (3)$$

where R_{calc} and R_{obs} are the calculated and observed mean line profiles (as a function of radial velocity ν) at phase ϕ with uncertainty σ , and λ is the Lagrange multiplier (see Collier Cameron 1992, for more details of Doppler imaging based on two-temperature model). SpotDIPy searches for the best Lagrange multiplier using the method suggested by Chiang et al. (2005), where minimum χ^2 and the entropy are calculated for each Lagrange multiplier during the optimization process. Then, the Lagrange multiplier that corresponds to the maximum curvature of the function χ^2 of entropy is used during the DI reconstruction. SpotDIPy uses L-BFGS-B algorithm (see Byrd et al. 1995; Zhu et al. 1997, for more details) to solve the bound constrained optimization problem, which is available in the SciPy³ library.

To test the robustness of SpotDIPy, we use DoTS as the comparison case, since the latter has been extensively used in the literature for DI purposes. In this context, using DoTS code, we generated synthetic line profiles with the S/N value of 500, including five spots with different sizes and locations, to simulate a spotted single

¹ github.com/phoebe-project/phoebe2

³ <https://scipy.org/>

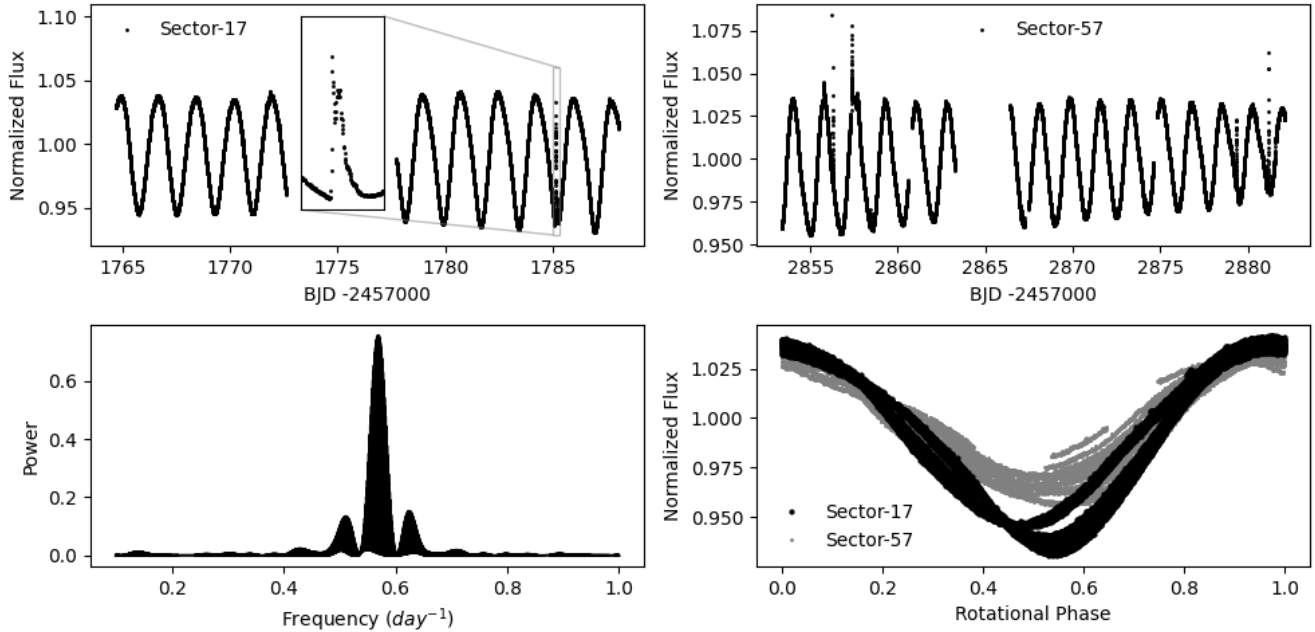


Figure 2. Top panel: TESS light curves in Sector 17 (left) and in Sector 57 (right). Bottom panel: Lomb-Scargle periodogram (left) and phase-folded light curves (right) using the period determined from the periodogram, for Sector 17 (black circles) and Sector 57 (gray circles).

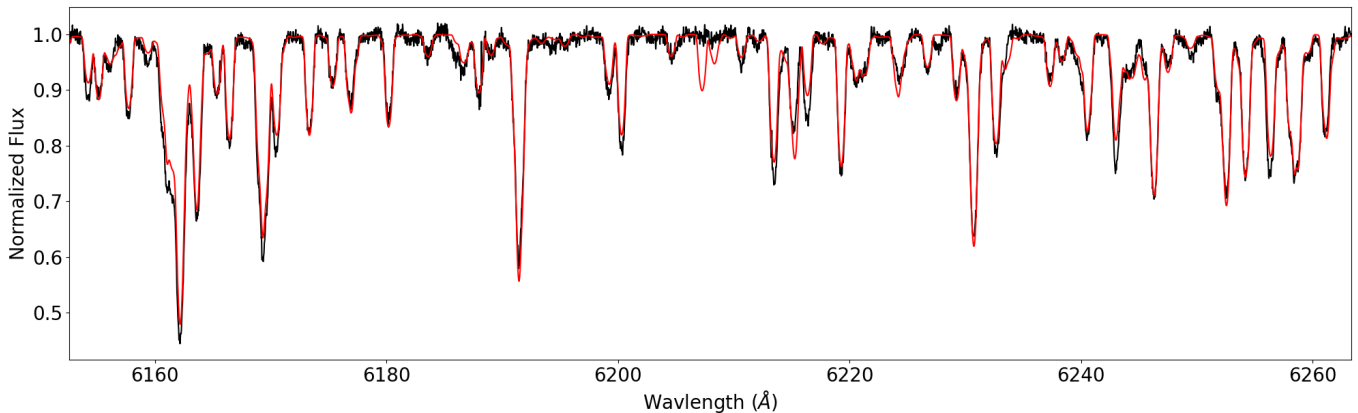


Figure 3. A comparison of the observed spectrum of PW And (black) with the best fit model (red) obtained through spectral synthesis fitting method.

star. We also assumed three different axial inclinations as 30° , 60° and 90° . The synthetic line profiles were generated with a sampling interval of 0.1 in phase. The stellar parameters were adopted as $v \sin i = 40 \text{ km s}^{-1}$, $mass = 1 M_\odot$ and $period = 1.5 \text{ days}$. These profiles were then used as input data for the surface reconstruction process performed using both DoTS and SpotDIPy. The surface grids for both codes were generated using 90 latitudinal zones that correspond to 180 surface elements along the equator, which is above the lower limit (80 surface elements) for the adopted $v \sin i$ value and the resolution ($R=150000$). Optimization was carried out

until the same χ^2 value is obtained in both codes as ~ 1 . Consequently, we calculated the standard deviations of the residuals, differences between models obtained from DoTS and SpotDIPy, in the order of 4.8×10^{-4} , 3.9×10^{-4} and 3.4×10^{-4} , for the three different axial inclination cases. The resultant maps generated by SpotDIPy are quite similar to those of DoTS, as seen in Figures 14, 15 and 16. Therefore, the test results showed that SpotDIPy can perform DI with the same accuracy as DoTS, for single stars.

In addition to the automatic calculation of the limb- and gravity-darkening coefficients, SpotDIPy also takes

into account the effects of macroturbulence and instrumental profile, unlike the DoTS code. `SpotDIPy` applies the macroturbulence broadening using the radial-tangential formulation adapted from SME (Valenti & Piskunov 1996). The instrumental profile is taken into account by convolving a kernel calculated over the given spectral resolution with the local line profiles, which is performed using the `PyAstronomy`⁴ (Czesla et al. 2019) Python package.

Molecular bands, such as Titanium Oxide (TiO), play a crucial role in providing precise assessments of spot coverage on the surfaces of stars. The area covered by cool spots as a percentage of the total stellar surface area can be determined through the analysis of molecular bands (Berdyugina 2002). In this context, We developed `SpotDIPy` to reconstruct surface maps by simultaneously utilizing both atomic lines and molecular band profiles. The reconstruction process of TiO-bands is the same as the DI process for atomic line profiles. The DI reconstruction process for TiO-bands is identical to that for atomic line profiles, with one notable distinction: in the TiO-band reconstruction process, the observed spectrum is directly matched with synthetic spectra determined by atmospheric parameters, representing the photosphere and spots without the need for an additional equivalent width correction.

3.4. Doppler Imaging of PW And

We performed the DI of PW And, using `SpotDIPy` for Set-1, Set-2 and Set-3 separately. The surface grid was selected in trapezoidal discretization mode. Using Eq. 9.1 of Kochukhov (2016), at least 12 resolution elements along the equator is sufficient to get a correctly reconstructed image for $v \sin i = 21.4$ and $R=85\,000$. However, we used 90 latitudinal zones corresponding to a total of 12,406 surface elements, for better visualization. The local line profiles are generated using the synthetic spectra that are derived from the stellar parameters provided in Table 2, which were employed to represent the quiet photosphere and spots, respectively. The same procedure was also applied to TiO-band region (7000-7100 Å). Atomic and molecular line list were extracted from VALD, while the synthetic spectra were generated using MARCS atmosphere models. We assumed the minimum spot temperature as 3800 K, which were given by Strassmeier & Rice (2006). The linear limb darkening coefficients (Kostogryz et al. 2022, 2023) were determined according to the effective temperature, the surface gravity and the metallicity of PW And. The gravity darkening effect were also considered using the

Eq. (31) of Espinosa Lara & Rieutord (2011). However, due to the relatively low equatorial rotational velocity of PW And, the gravity darkening has no significant effect on the observed profiles.

It is also possible to fine-tune the stellar parameters (e.g. $v \sin i$), using χ^2 minimization within `SpotDIPy`. As the preliminary stellar parameters for DI, we used those given in Table 2. `SpotDIPy` uses an additional equivalent-width parameter (called EW), which affects the widths and depths of the local line profiles generated using synthetic spectra. EW thus allows us to control the depth of the LSD profiles, which are also critical to circumvent DI artifacts, such as spurious polar spots (Collier Cameron & Unruh 1994). To optimize EW , we carried out a two-dimensional grid search on the $EW - v \sin i$ plane, using the χ^2 minimization feature of `SpotDIPy`, where the algorithm searches for minimum χ^2 for a particular value of the Lagrange multiplier, for each pair of $EW - v \sin i$ parameters. Contour plots of the resulting χ^2 for 3 sets are shown in Figure 4. The minimum χ^2 values turned out to be at $v \sin i = 21.5^{+1.4}_{-1.3}$ km s⁻¹ for Set-1, $21.3^{+2.2}_{-1.5}$ km s⁻¹ for Set-2, $21.3^{+1.1}_{-1.3}$ km s⁻¹ for Set-3. The errors of the $v \sin i$ parameters were estimated from $\chi^2_{min} + 1$ of $v \sin i$ values obtained from 2D grid search (see Bevington & Robinson 2003, for more details). The average $v \sin i$ was calculated as $21.4^{+1.0}_{-0.8}$ km s⁻¹, which is slightly lower than the one determined by Strassmeier & Rice (2006) and almost the same as found by Llorente de Andrés et al. (2021). The adopted stellar parameters used in DI are listed in Table 2. The LSD profiles, TiO-band profiles, and their respective best-fit models for all datasets are illustrated in Figure 5, Figure 6-8, respectively. It is evident from the the Figure 5 and Figure 6-8 that the models obtained through DI are highly compatible with both LSD and TiO molecular band profiles. The Mollweide projections of the resulting DI maps for Set-1, Set-2 and Set-3 are shown in Figure 9.

Map of Set-1 shows a high-latitude spot region centered at about latitude 75° and mid-latitude spots distributed around 30° latitude. Set-2 and Set-3 show similar latitudinal distributions seen in the map of Set-1, with a predominant high-latitude spot and other spots spread over mid-latitudes, particularly around 30° latitude. Although there is almost a 3-year time span between Set-1 and Set-2-3, the longitudinal distributions of starspots also show similarities, with the exception of a jump in longitude of the high-latitude spot from 2015 to 2018. The same feature is found roughly at the same longitude but with a different size when comparing Set-2 and Set-3 maps.

⁴ <https://github.com/sczesla/PyAstronomy>

Table 2. Adopted stellar parameters.

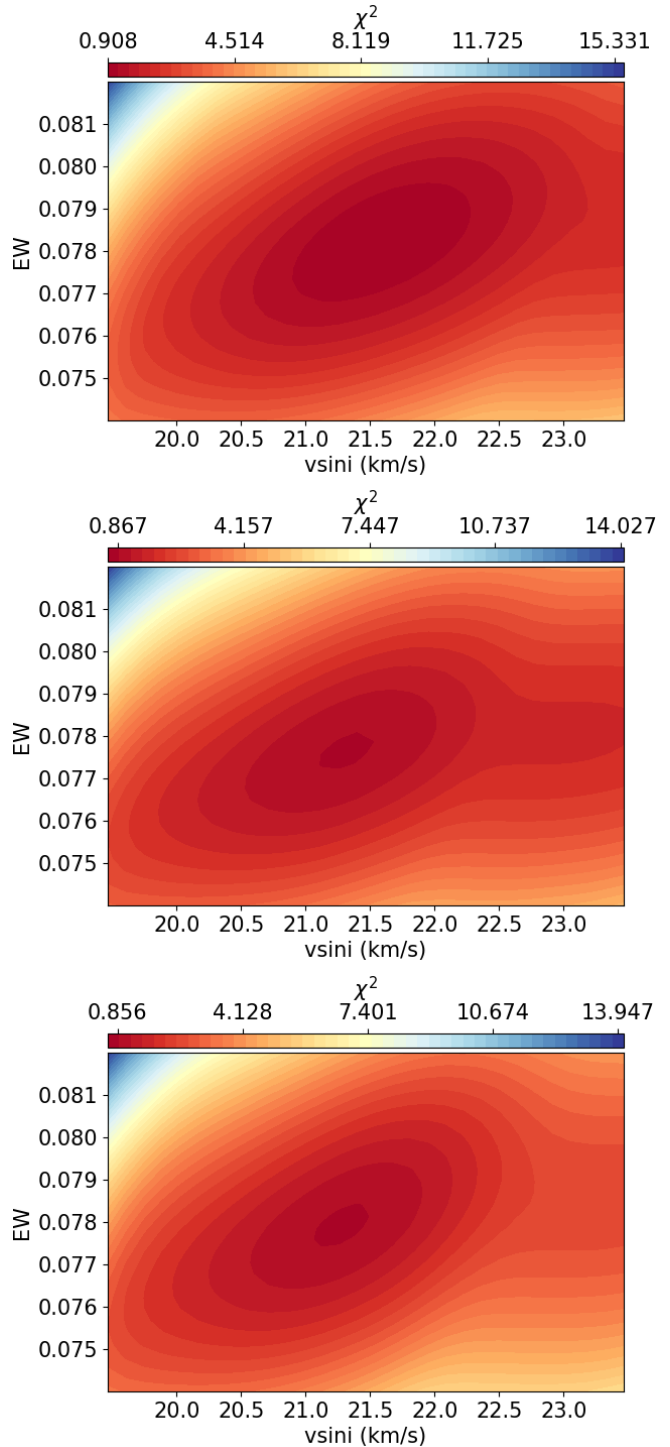
Parameter	Value
$v \sin i$ [km/s]	$21.4^{+1.0}_{-0.8}$ ^a
M [M_{\odot}]	0.85 ± 0.05 ^b
i [$^{\circ}$]	46.0 ± 7 ^c
P_{rot} [day]	1.756604 ± 0.000015 ^a
T_0 [HJD]	2453200.0 ^c
T_{eff} [K]	5080 ± 28 ^a
T_{spot} [K]	3800 ^c
$\log g$	4.40 ± 0.09 ^a
[Fe/H]	-0.14 ± 0.02 ^a
ξ [km/s]	1.93 ± 0.09 ^a
ζ [km/s]	3.25 ± 0.06 ^a

^a This study.^b Folsom et al. (2016).^c Strassmeier & Rice (2006).

The latitudinal distributions we found for all set of maps are clearly different from the surface map obtained by Strassmeier & Rice (2006), which showed dominated low-latitude spots between $+40^{\circ}$ and -20° . A similar result was obtained by Kolbin & Galeev (2017), who found spots covering latitudes from 30° to 60° . The surface maps obtained by Gu et al. (2010), on the other hand, exhibited a very large high-latitude spot, which extends to intermediate latitudes, making it a much more similar pattern with those in Figure 9.

The number of rotational cycles included in the spectroscopic data is a crucial factor to consider when generating DI maps. This is especially important when accounting for short-term magnetic evolution and/or a high differential rotation rate, as it can influence the presence of artificial features in the resulting maps. In the study conducted by Gu et al. (2010), the maps were reconstructed using spectroscopic data that covered approximately 13.7 and 8.6 rotational cycles for subset 1 and subset 2, respectively. It is essential to acknowledge that reconstructed maps may exhibit artifacts due to the inclusion of spectroscopic data with relatively high rotation cycles. On the other hand, Strassmeier & Rice (2006) and Kolbin & Galeev (2017) utilized spectroscopic data encompassing approximately 3.4 and 4.6 rotation cycles, respectively. Considering Set-1, Set-2, and Set-3 data used in this study, these values decrease to 2.9, 2.4, and 2.3, respectively. Such lower number of rotational cycles are more conducive to DI, as they reduce the likelihood of significant artificial features being introduced into the maps.

3.5. Chromospheric Activity Indicators

**Figure 4.** 2D grid search on the $EW-v \sin i$ plane for Set-1 (top), Set-2 (middle) and Set-3 (bottom). The colors show the χ^2 values.

The presence of chromospheric activity on PW And is known since the work by Bidelman (1985), who confirmed the existence of moderate emission in Ca II H&K lines. One of the most detailed chromospheric activ-

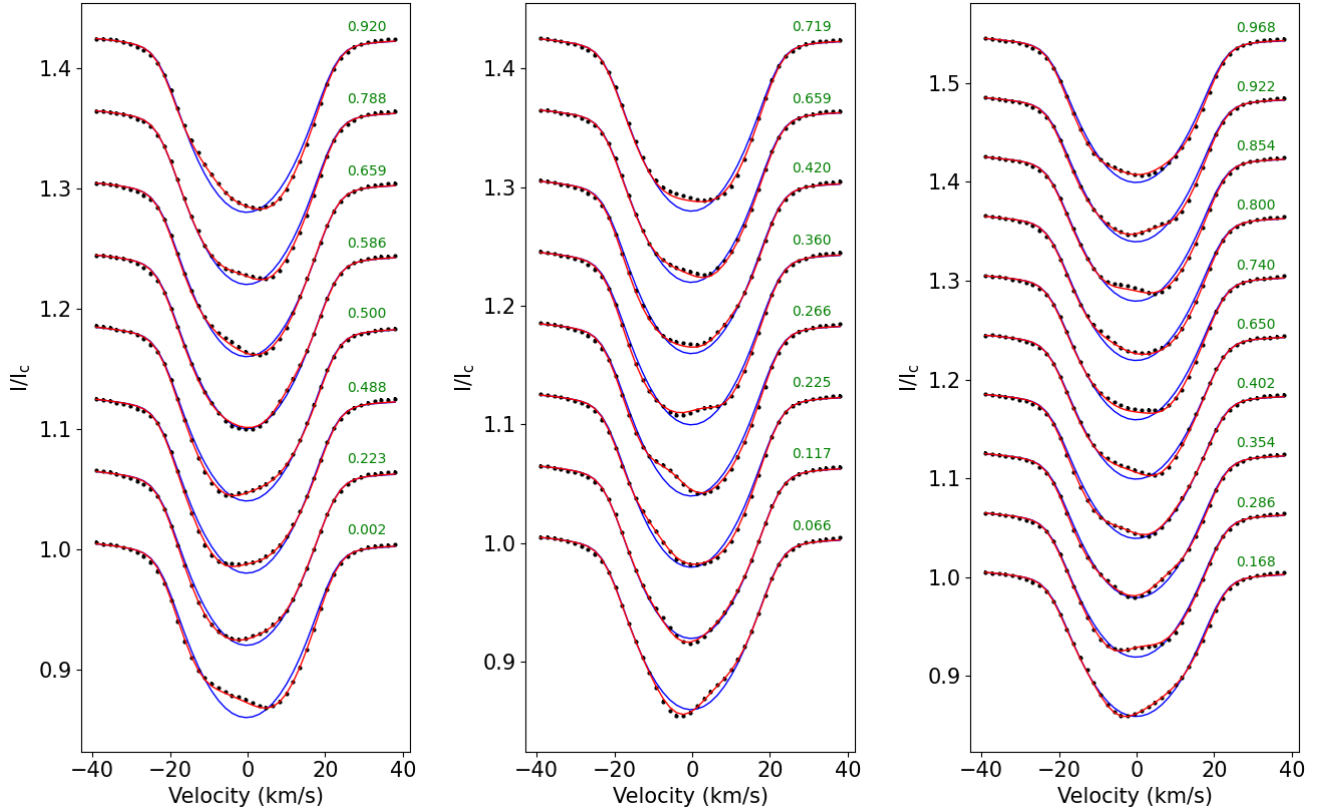


Figure 5. Phase-ordered LSD profiles (filled circles) with the error bars derived from the observed spectra, the spotless synthetic line profiles (blue solid lines) and the best fit models (red solid lines) generated by the reconstruction process. The left, middle, and right panels are for Set-1, Set-2 and Set-3, respectively.

ity investigation of PW And was carried out by López-Santiago et al. (2003), who used all chromospheric indicator lines in the optical range by employing the spectral subtraction technique and mentioned that Balmer lines are clearly visible in emission in the subtracted spectra. Depending on the ratio of $EW(H_\alpha)$ and $EW(H_\beta)$ López-Santiago et al. (2003) argued that the emission of these lines could arise from prominence-like material, whereas the ratio of the excess emission of two Ca II lines (8498 Å and 8542 Å) arise from plage-like regions. Employing the spectral subtraction technique to H_α and Ca II IRT lines, Zhang et al. (2015) obtained similar findings concerning the strong magnetic activity of PW And.

Following the chromospheric activity results in the literature, we investigate the rotational modulation of PW And’s chromospheric excess emission, by applying the same method, spectral subtraction, for Ca II H&K, H_α , and Ca II IRT lines. By ‘excess emission’, we hereafter mean the line emission left when the adapted synthetic spectrum obtained using the same stellar parameters of PW And was subtracted. We artificially broadened its spectral lines to the $v \sin i$ value of PW And, 21.4 km s^{-1} . We then subtracted the result-

ing continuum-normalized spectrum from each PW And spectrum. Comparisons of PW And Ca II H&K, H_α and Ca II IRT spectra with those from the synthetic spectrum are shown in Figure 10. Next, we measured the excess equivalent width (hereafter EEQW) in the Ca II H&K ($\lambda 3968$ and $\lambda 3933$), H_α ($\lambda 6563$) and Ca II IRT lines ($\lambda 8498$, $\lambda 8542$, and $\lambda 8662$) of the subtracted spectra, by integrating over above the zero level of the subtracted profiles. We estimated uncertainties of the EEQWs, using the equation 2.3 of Schöfer (2021). All EEQW measurements are listed in Table 3. The EEQW variations of Ca II H&K, H_α and Ca II IRT emissions along with the rotational phase for each data-set that are shown in Figure 13 show similar trends among themselves. In Set-1, there is an abrupt increase in the EEQWs of all chromospheric emissions, observed during phase 0.659. A very similar phenomenon is evident for phase 0.420 of Set-2, for which the emission peaks also have distinctly higher values compared to the general trend. As a rapidly rotating K2 V star, PW And is expected to have strong flare activity. Two such flares were detected by López-Santiago et al. (2003), who were able to observe the entire pre-flare, flare and the gradual decay phases. To inspect a possible connection of abrupt

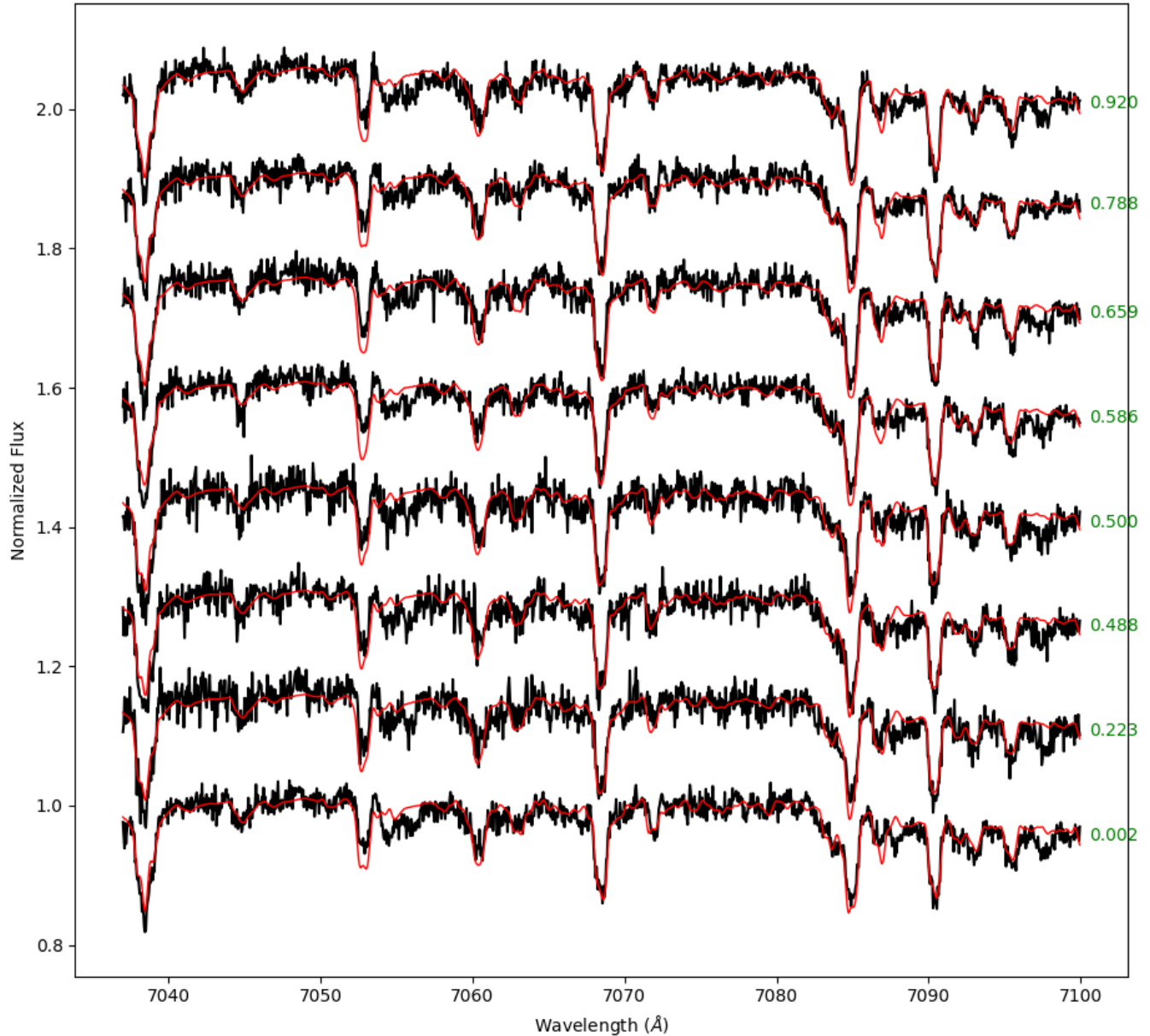


Figure 6. Phase-ordered TiO-band profiles (black solid lines) of Set-1 and the best fit models (red solid lines) generated by the DI process.

increases in the EEQWs to flare activity, we measured the chromospheric flare-diagnostic lines He I D₃ and the Na I doublet. Following spectral subtraction, we found them in excess emission, as seen from Figure 11. Therefore, we conclude that the two spectra that correspond to phases 0.659 and 0.420 of Set-1 and Set-2 data may be observed during pre-flare, flare or the gradual decay phases.

4. CONCLUSION AND DISCUSSION

In this study, we analyzed high-resolution spectra of PW And considering three datasets obtained in different

observing seasons, to investigate the activity nature of the star, using different methods. We also presented the most recent and accurate rotation period of PW And determined from the precise and almost continuous TESS light curves, by computing the Lomb-Scargle periodogram. The photospheric activity was investigated using the DI technique to reconstruct starspot distributions. This was achieved by simultaneously modeling both atomic line and TiO molecular band profile, utilizing a new Python-based DI code called `SpotDIPy`.

DI maps derived from Set-1, Set-2, and Set-3 data clearly show a dominant high-latitude spot as well as

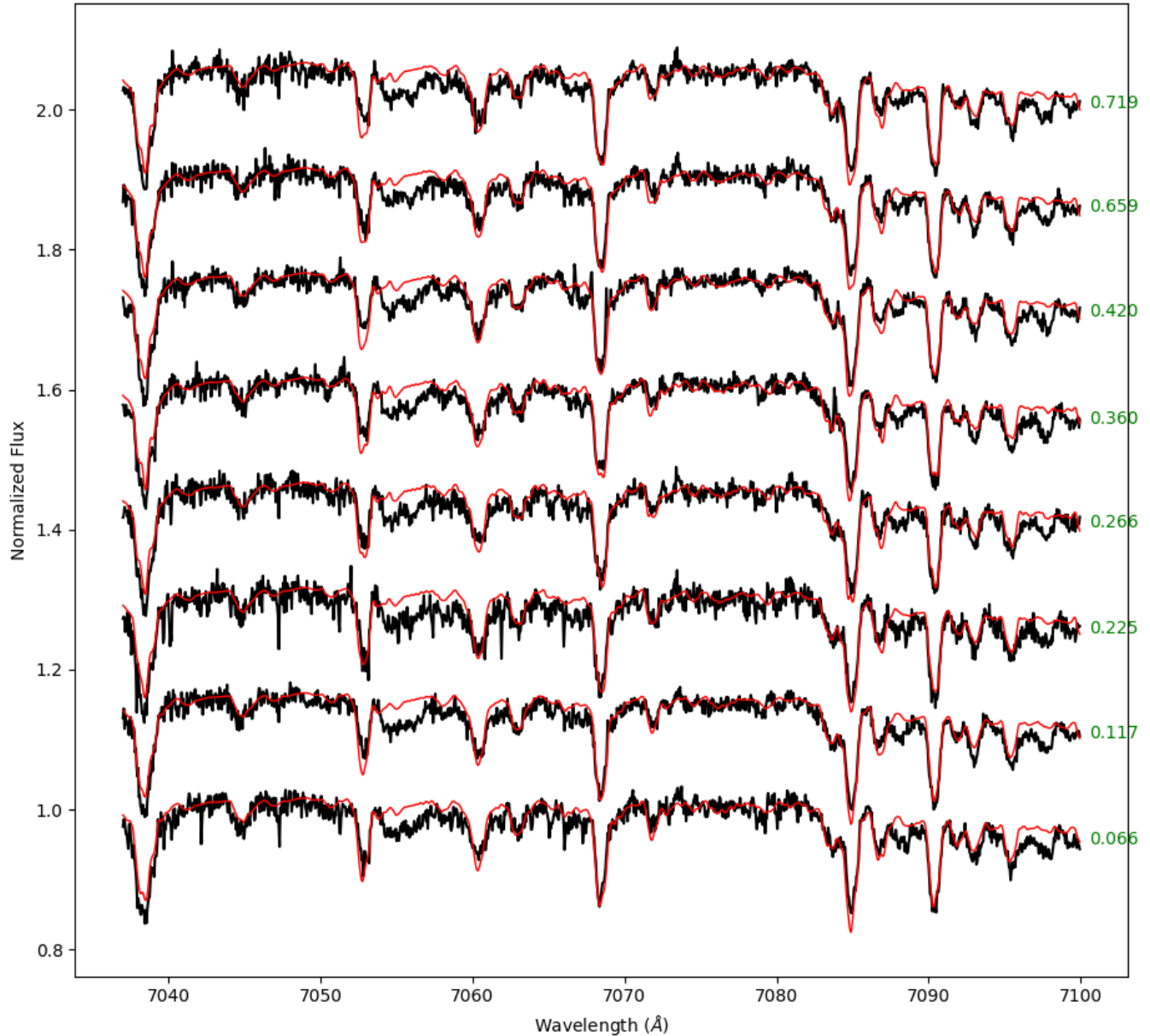


Figure 7. Same as Figure 6, but for Set-2

mid- to low-latitude spots down to $\sim +30^\circ$ latitudes. It is remarkable that the high-latitude spot continues to exist, in spite of a three-year time span between Set-1 and Set-2-3. The TESS light curves, also spanning three years, exhibit almost the same light-curve characteristics as magnetic flux continuously emerges and decays within the same phase range over the entire time span, during which one longitude region is dominant (see Figure 2). [López-Santiago et al. \(2003\)](#) obtained the same finding using the CCF technique and mentioned that the variations of CCF bisectors found in three epochs reveal the prevalence over time of large spots or the existence of

active longitudes where spots are continuously emerge. We compared the resulting surface maps of Set-1, Set-2 and Set-3 in Figure 12. It can be clearly seen that the high-latitude spot of Set-1 is located on lower longitudes than that of Set-2, while the high-latitude spots in Set-2-3 were almost centered on the same longitude. Therefore, considering (a) the explanation by [López-Santiago et al. \(2003\)](#), (b) the TESS light curves and (c) the DI maps presented in this study, the most plausible explanation for the main component of variability in PW And is the prevalence of large spots or spot groups over time. Moreover, this might indicate that differential rotation

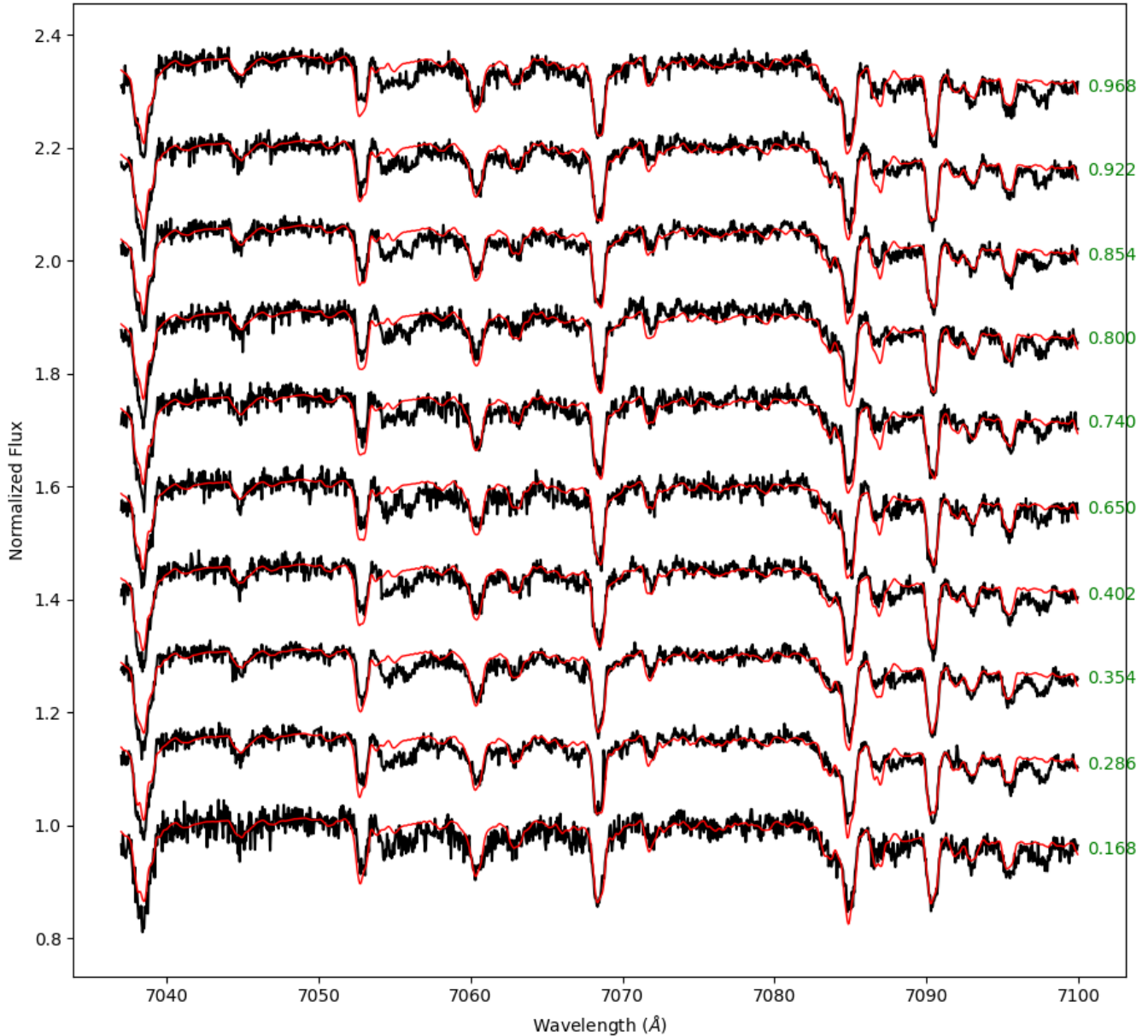


Figure 8. Same as Figure 6, but for Set-3

is minimal on PW And and future observations spanning more rotation cycles could be used to place firm limits on this.

We conducted some tests to investigate the impact of S/N and phase coverage on the maps obtained for PW And. In this context, an artificial map was created with the spot distribution seen in the top panel of Figure 17 and artificial line profiles were generated based on the stellar parameters of PW And using this map. In the first test, we compared the maps obtained using line profiles having the same average S/N value and the phase coverage of Set-1, with the maps gener-

ated via the line profiles using the same S/N value but with a 0.05 phase interval. In the second test, unlike the first one, we compared the maps obtained from line profiles with significantly higher S/N values (Figure 17). As can be seen from the resultant maps, relatively low S/N and insufficient phase coverage provide lower spot coverage than expected. Additionally, depending on the axial inclination, spots near the unseen latitudes of the stellar surface tend to have latitudes higher than what is expected. Therefore, when considering S/N and phase coverage in PW And observations, it can be said that the total spot coverage may be underestimated to some

Table 3. Measurements of EEQWs of Ca II H&K, H α and Ca II IRT.

BJD _{Mid}	Ca II				Ca II IRT	
	K	H	H α	λ 8498	λ 8542	λ 8662
57371.33485	0.866 \pm 0.117	1.055 \pm 0.126	1.249 \pm 0.071	0.595 \pm 0.060	0.775 \pm 0.039	0.627 \pm 0.028
57372.32557	0.873 \pm 0.101	1.050 \pm 0.126	1.252 \pm 0.083	0.515 \pm 0.063	0.683 \pm 0.038	0.563 \pm 0.045
57373.31892	0.916 \pm 0.131	0.943 \pm 0.133	0.919 \pm 0.063	0.458 \pm 0.067	0.579 \pm 0.040	0.488 \pm 0.028
57375.30687	0.846 \pm 0.062	1.023 \pm 0.083	0.910 \pm 0.070	0.461 \pm 0.063	0.605 \pm 0.035	0.493 \pm 0.029
57375.45063	0.791 \pm 0.122	1.072 \pm 0.147	0.904 \pm 0.075	0.481 \pm 0.059	0.627 \pm 0.036	0.507 \pm 0.023
57376.30420	0.873 \pm 0.085	1.115 \pm 0.098	1.127 \pm 0.081	0.501 \pm 0.059	0.613 \pm 0.049	0.524 \pm 0.043
57376.32586	0.864 \pm 0.162	1.049 \pm 0.165	1.130 \pm 0.078	0.478 \pm 0.052	0.633 \pm 0.050	0.519 \pm 0.035
57376.47667	0.759 \pm 0.062	0.991 \pm 0.094	1.006 \pm 0.068	0.456 \pm 0.063	0.591 \pm 0.038	0.491 \pm 0.027
58387.36672	1.009 \pm 0.094	1.135 \pm 0.115	0.678 \pm 0.069	0.399 \pm 0.059	0.560 \pm 0.037	0.444 \pm 0.023
58387.45742	0.963 \pm 0.086	1.248 \pm 0.141	0.765 \pm 0.065	0.412 \pm 0.061	0.552 \pm 0.033	0.442 \pm 0.024
58388.40970	0.854 \pm 0.124	1.063 \pm 0.121	0.637 \pm 0.060	0.410 \pm 0.059	0.558 \pm 0.039	0.445 \pm 0.021
58388.51470	1.193 \pm 0.104	1.479 \pm 0.125	0.772 \pm 0.064	0.423 \pm 0.057	0.564 \pm 0.033	0.456 \pm 0.023
58389.40298	0.832 \pm 0.086	1.146 \pm 0.119	0.788 \pm 0.066	0.423 \pm 0.062	0.567 \pm 0.036	0.459 \pm 0.028
58389.47599	0.909 \pm 0.096	1.142 \pm 0.129	0.789 \pm 0.071	0.405 \pm 0.063	0.567 \pm 0.030	0.465 \pm 0.025
58391.39727	0.811 \pm 0.053	1.060 \pm 0.085	0.904 \pm 0.062	0.442 \pm 0.061	0.595 \pm 0.031	0.469 \pm 0.027
58391.50205	0.841 \pm 0.054	1.057 \pm 0.090	1.530 \pm 0.050	0.658 \pm 0.056	0.836 \pm 0.030	0.706 \pm 0.016
58467.44046	0.936 \pm 0.113	1.168 \pm 0.151	0.706 \pm 0.071	0.446 \pm 0.063	0.601 \pm 0.034	0.495 \pm 0.028
58468.35045	0.946 \pm 0.159	1.134 \pm 0.148	1.097 \pm 0.085	0.445 \pm 0.075	0.586 \pm 0.046	0.471 \pm 0.045
58469.35515	0.801 \pm 0.100	1.107 \pm 0.140	0.740 \pm 0.072	0.415 \pm 0.056	0.566 \pm 0.030	0.470 \pm 0.025
58469.46048	0.799 \pm 0.077	1.025 \pm 0.096	0.831 \pm 0.075	0.432 \pm 0.061	0.585 \pm 0.039	0.472 \pm 0.020
58470.31374	1.375 \pm 0.056	1.880 \pm 0.098	0.937 \pm 0.070	0.438 \pm 0.068	0.595 \pm 0.042	0.481 \pm 0.017
58470.43395	0.867 \pm 0.069	1.135 \pm 0.094	0.915 \pm 0.061	0.425 \pm 0.060	0.560 \pm 0.044	0.467 \pm 0.020
58470.51817	0.837 \pm 0.048	1.171 \pm 0.097	0.868 \pm 0.062	0.419 \pm 0.062	0.555 \pm 0.034	0.444 \pm 0.023
58471.31222	0.948 \pm 0.158	1.064 \pm 0.194	0.814 \pm 0.071	0.426 \pm 0.062	0.566 \pm 0.035	0.469 \pm 0.023
58471.43170	1.112 \pm 0.166	1.208 \pm 0.177	0.823 \pm 0.072	0.401 \pm 0.065	0.570 \pm 0.034	0.434 \pm 0.021
58471.51305	0.953 \pm 0.162	1.055 \pm 0.167	0.874 \pm 0.063	0.426 \pm 0.063	0.578 \pm 0.036	0.466 \pm 0.022

extent and the latitudes of low-latitude spots may be somewhat overestimated.

The obtained spot distributions from DI are compatible with those of Gu et al. (2010). On the other hand, Strassmeier & Rice (2006) claimed that the spots on PW And are distributed between $+40^\circ$ and -20° latitude without the presence of a high-latitude spot. Gu et al. (2010), explained the reason for the large difference between the surface maps reconstructed by them and Strassmeier & Rice (2006) as the lifetime of main spot structure cannot last more than one year and should change largely during its one activity cycle, similar to LQ Hya. Besides, a K0-type star's convection zone has a larger fractional depth compared to that of a solar-mass star. When combined with the strong Coriolis effect, this results in higher emergence latitudes and strong polar magnetic fields (Işık et al. 2011), which is in accordance with the spot distributions reconstructed for PW And in this study.

We show a comparison of DI-based f_s variations along with the chromospheric diagnostics for all sets in Figure 13. The EEQW variations of H α , Ca II H&K and Ca II IRT emissions for the entire dataset show almost the same trend among themselves. Besides, the flare event seen during Set-1 and Set-2 is clearly traceable from the abrupt increase in EEQWs of all indicator lines. It should be noted that there is almost 2.5 hours between phases 0.360 and 0.420, where the latter corresponds to a possible flare event. López-Santiago et al. (2003) mentioned that there is approximately 24 hours between the flare event and the pre-flare phase during their spectral observations of PW And. Therefore, the spectrum taken during phase 0.360 most likely corresponds to the pre-flare event.

The EEQW variation of Ca II H&K and Ca II IRT lines show very similar trends to DI f_s characteristics, while variation of EEQWs for H α differs slightly. Compared to the f_s variations from DI, the chromospheric diagnostics show discrepancies due to the strong flare

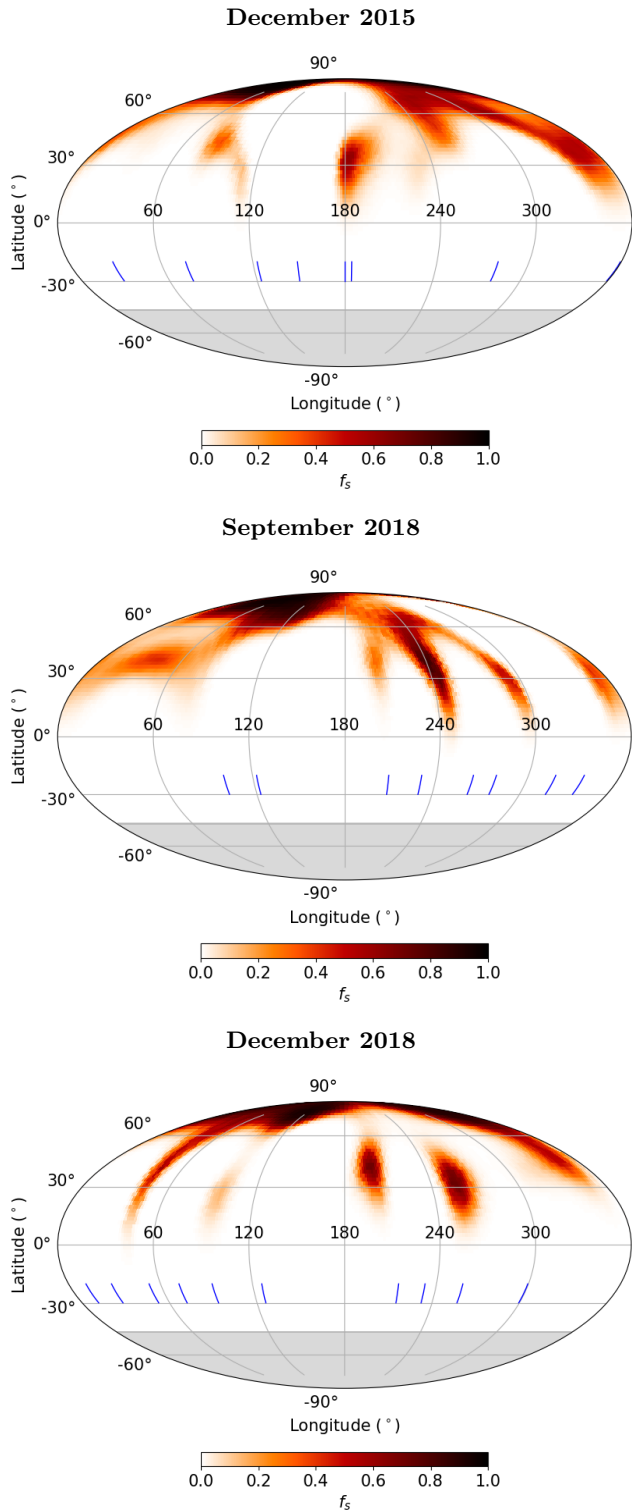


Figure 9. Mollweide projections of the reconstructed maps of PW And in terms of spot filling factors. First three panels from top to bottom show map of Set-1, Set-2 and Set-3, respectively. The tick marks in the Mollweide projection show the phase coverage of spectral data. The shaded region around the south pole of the projection indicates unseen region of PW And's surface, due to the axial inclination.

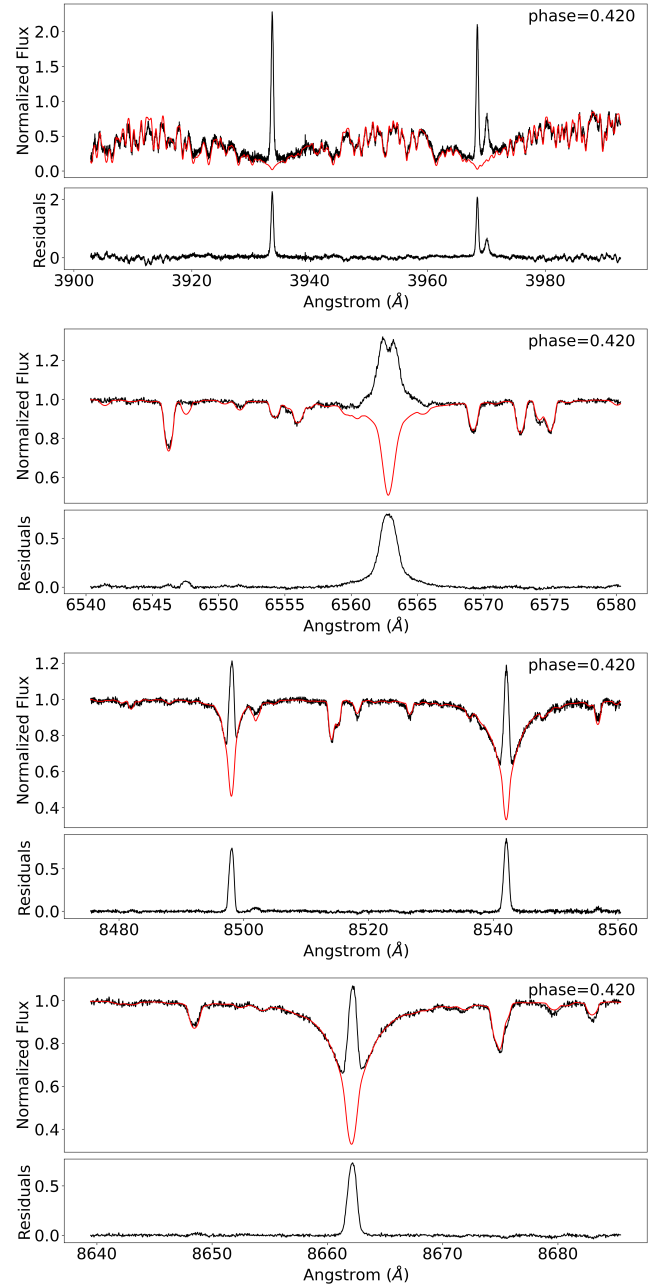


Figure 10. An example of spectral subtraction of Ca II H&K, H α and Ca II IRT lines at the rotational phase 0.413 in the Set-2. The red solid lines show the synthesized spectrum of HD 166620. The black solid lines above and below show the observed and subtracted spectra in each panel, respectively.

event in Set-2. The chromospheric excess emission variations are also in parallel with the f_s variations obtained from DI in Set-3, although the Ca II H&K and Ca II IRT are more scattered. Our findings imply that PW And's chromospheric activity patterns are spatially associated with its starspots.

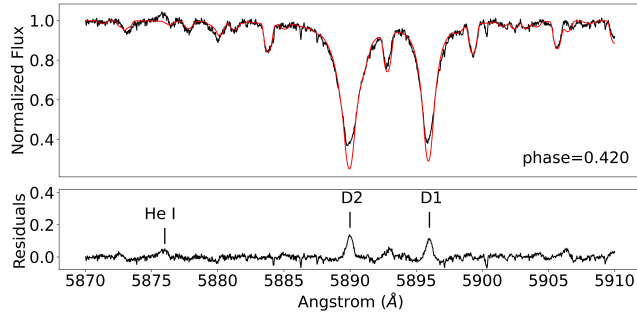


Figure 11. Excess emissions of He I D₃, Na I (D₁, D₂) lines at phase 0.413 of Set-2.

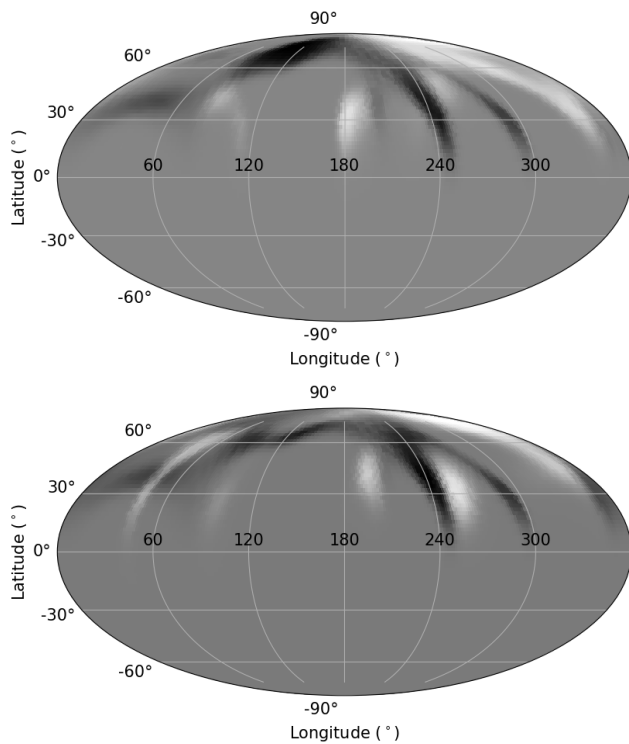


Figure 12. Comparison of the maps reconstructed using Set-1, Set-2, and Set-3. In both panels, black indicates the predominance of spot regions from Set-2. White indicates the predominance of spot regions from Set-1 and Set-3 in upper and lower panel, respectively.

Molecular bands, such as TiO-bands, offer valuable insights into the examination of cool spots on the surfaces of active stars. However, achieving precise modeling of molecular bands requires the consideration of especially the actual elemental abundances as well as the Doppler shifts to obtain a more accurate evaluation of spot coverage on stellar surfaces. In the study by Berdyugina (2002), synthetic TiO-band profiles generated from the spot distribution obtained through DI

analysis of 6 atomic line profiles at 11 different rotational phases of IM Peg are seen to be in excellent agreement with the observed TiO-band profiles, proving that the recovered spot coverage from the atomic lines are reliable. In this study, a simultaneous DI process was employed to effectively model both the atomic lines (LSD profiles) and the TiO-band profiles at 7055 Å of PW And (see Figures 5, 6, 7 and 8). The average S/N values obtained for atomic lines (LSDs) from Set-1, Set-2, and Set-3 are 732, 811, and 766, respectively, while for TiO-band profiles, they are 86, 118, and 100. This implies that during inversion, atomic lines have 8.5, 6.9, and 7.7 times more weight compared to molecular band profiles. Therefore, it is clear that TiO-bands exhibit significantly lower signal-to-noise ratios compared to LSD profiles, thereby giving the latter a more substantial weight on the resulting surface spot distributions in simultaneous DI processes. Nevertheless, the successful modeling of TiO-bands performed in this study validates the accuracy of the spot distributions derived from these simultaneous analyses, as also achieved by Berdyugina (2002). Therefore, in order to precisely determine the spot characteristics, the DI and TiO should be considered simultaneously.

We introduced a new Python-based DI code, SpotDIPy that is able to reconstruct the surface brightness distribution of single stars based on two temperature approximation. SpotDIPy was tested with the help of some simulations in comparison with the well-known DI code DoTS. The test results showed that SpotDIPy gave almost identical maps as those obtained via DoTS in terms of reconstructing surface brightness distribution of stars, indicating the success of the code SpotDIPy. SpotDIPy is an open source code that allows other users to modify and develop it freely. It is user-friendly with certain plotting GUI capabilities and is simple to use. In the near future we plan to adopt SpotDIPy for binary stars and also to provide a surface reconstruction option for the temperature distribution of stars. The code will be accessible on GitHub⁵ by the end of 2023.

We would like to thank the referee, Dr. Klaus Strassmeier, whose critical comments led to substantial improvement of the manuscript. HVS acknowledges the support by The Scientific And Technological Research Council Of Türkiye (TÜBİTAK) through the project 1001 - 115F033. DM acknowledges financial support from the Agencia Estatal de Investigación of the Ministerio de Ciencia, Innovación through project PID2019-

⁵ <https://github.com/EnginBahar/SpotDIPy>

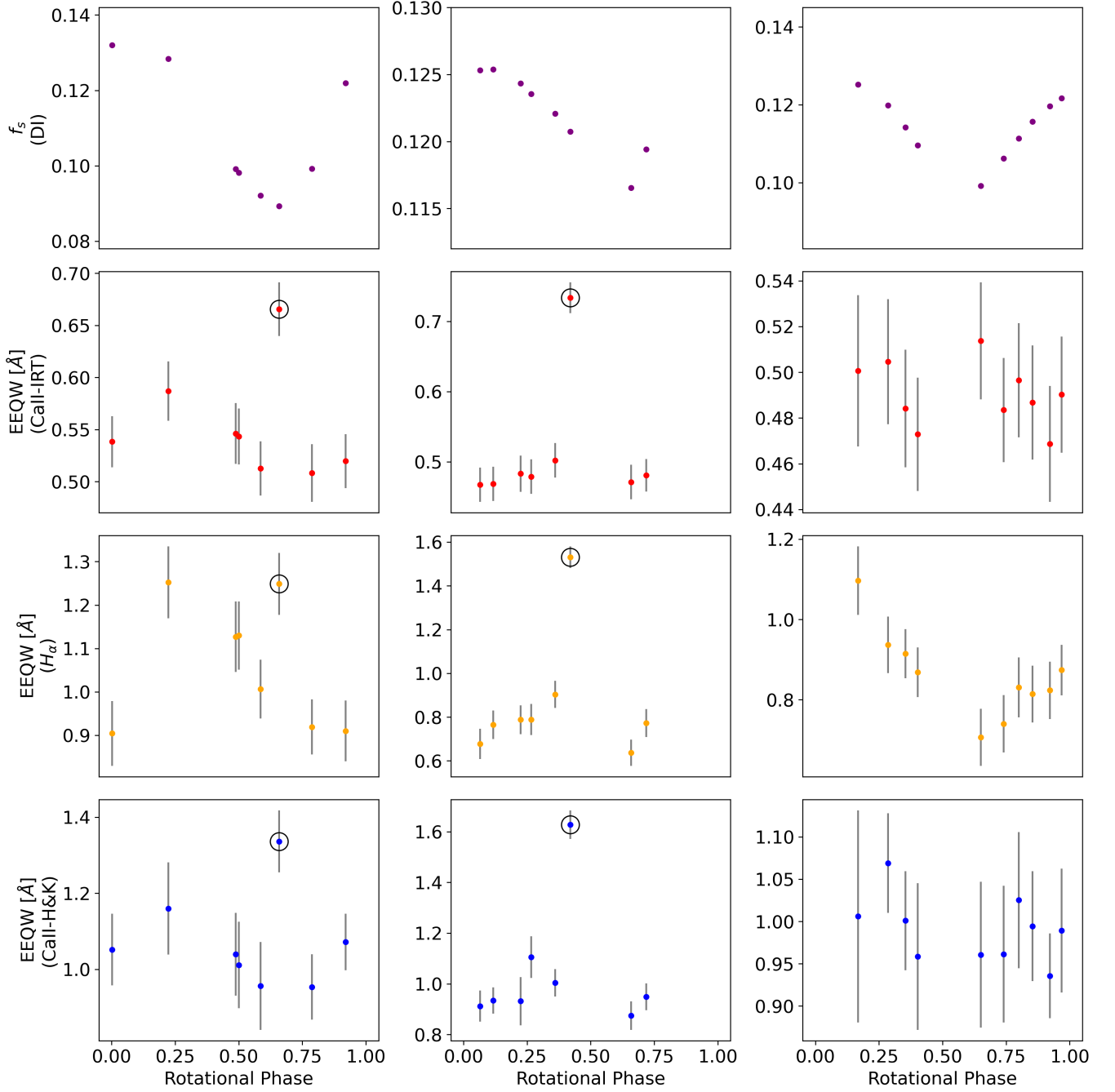


Figure 13. Comparison of photospheric and chromospheric activity induced rotational modulations. First row shows photospheric rotational modulations arising from cool spots obtained from DI. Third row shows EEQW variations of H_α lines, while second and last rows show averaged EEQW variations of Ca II IRT and Ca II H&K lines, respectively. From left to right, each column represents Set-1, Set-2 and Set-3 data, respectively. Large open circles denote flare events.

109522GB-C5[4]/AEI/10. OK acknowledges support by the Swedish Research Council (project 2019-03548).

Software: DoTS (Collier Cameron 1992), SpotDIPy (Bahar 2023), ExoTiC-LD (Grant & Wakeford 2022),

PHOEBE2 (Prša et al. 2016), SciPy (Virtanen et al. 2020), PyAstronomy (Czesla et al. 2019), Numpy (Harris et al. 2020), Autograd (Maclaurin et al. 2015), Kneebow (Georg 2019), Astropy (Astropy Collaboration et al. 2013, 2018, 2022), PyQt (PyQT 2012), Matplotlib (Hunter 2007), Mayavi (Ramachandran & Varoquaux 2011)

REFERENCES

- Astropy Collaboration, Robitaille, T. P., Tollerud, E. J., et al. 2013, *A&A*, 558, A33
- Astropy Collaboration, Price-Whelan, A. M., Sipőcz, B. M., et al. 2018, *AJ*, 156, 123
- Astropy Collaboration, Price-Whelan, A. M., Lim, P. L., et al. 2022, *apj*, 935, 167
- Bahar, E. 2023, SpotDIPy, vv0.0.1-alpha, Zenodo, doi:10.5281/zenodo.8386064. <https://zenodo.org/badge/latestdoi/590005896>
- Berdugina, S. V. 2002, *Astronomische Nachrichten*, 323, 192
- Bevington, P. R., & Robinson, D. K. 2003, *Data reduction and error analysis for the physical sciences*
- Bidelman, W. P. 1985, *AJ*, 90, 341
- Blanco-Cuaresma, S. 2019, *MNRAS*, 486, 2075
- Blanco-Cuaresma, S., Soubiran, C., Heiter, U., & Jofré, P. 2014, *A&A*, 569, A111
- Byrd, R. H., Lu, P., Nosedal, J., & Zhu, C. 1995, *SIAM Journal on Scientific Computing*, 16, 1190
- Şenavcı, H. V., Bahar, E., Montes, D., et al. 2018, *MNRAS*, 479, 875
- Chiang, Y.-W., Borbat, P. P., & Freed, J. H. 2005, *Journal of Magnetic Resonance*, 177, 184
- Collier Cameron, A. 1992, in *Lecture Notes in Physics*, Berlin Springer Verlag, Vol. 397, *Surface Inhomogeneities on Late-Type Stars*, ed. P. B. Byrne & D. J. Mullan, 33
- Collier Cameron, A., & Unruh, Y. C. 1994, *MNRAS*, 269, 814
- Czesla, S., Schröter, S., Schneider, C. P., et al. 2019, *PyA: Python astronomy-related packages*, , ascl:1906.010
- Dempsey, R. C., Bopp, B. W., Strassmeier, K. G., et al. 1992, *ApJ*, 392, 187
- Donati, J.-F., Semel, M., Carter, B. D., Rees, D. E., & Collier Cameron, A. 1997, *MNRAS*, 291, 658
- Espinosa Lara, F., & Rieutord, M. 2011, *A&A*, 533, A43
- Folsom, C. P., Petit, P., Bouvier, J., et al. 2016, *MNRAS*, 457, 580
- Georg, U. 2019, *kneebow: Knee or elbow detection for curves*, <https://github.com/georg-un/kneebow>, ,
- Grant, D., & Wakeford, H. R. 2022, *Exo-TiC/ExoTiC-LD: ExoTiC-LD v3.0.0, vv3.0.0*, Zenodo, doi:10.5281/zenodo.7437681. <https://doi.org/10.5281/zenodo.7437681>
- Gray, R. O., & Corbally, C. J. 1994, *AJ*, 107, 742
- Griffin, R. F. 1992, *The Observatory*, 112, 41
- Gu, S.-h., Collier Cameron, A., & Kim, K. M. 2010, in *IAU Symposium*, Vol. 264, *Solar and Stellar Variability: Impact on Earth and Planets*, ed. A. G. Kosovichev, A. H. Andrei, & J.-P. Rozelot, 90–92
- Gustafsson, B., Edvardsson, B., Eriksson, K., et al. 2008, *A&A*, 486, 951
- Harris, C. R., Millman, K. J., van der Walt, S. J., et al. 2020, *Nature*, 585, 357. <https://doi.org/10.1038/s41586-020-2649-2>
- Hunter, J. D. 2007, *Computing in Science & Engineering*, 9, 90
- İşık, E., Schmitt, D., & Schüssler, M. 2011, *A&A*, 528, A135
- Kochukhov, O. 2016, in *Lecture Notes in Physics*, Berlin Springer Verlag, Vol. 914, *Lecture Notes in Physics*, Berlin Springer Verlag, ed. J.-P. Rozelot & C. Neiner, 177
- Kolbin, A. I., & Galeev, A. I. 2017, in *Astronomical Society of the Pacific Conference Series*, Vol. 510, *Stars: From Collapse to Collapse*, ed. Y. Y. Balega, D. O. Kudryavtsev, I. I. Romanyuk, & I. A. Yakunin, 417
- Kostogryz, N., Shapiro, A., Witzke, V., et al. 2023, *Research Notes of the AAS*, 7, 39
- Kostogryz, N., Witzke, V., Shapiro, A., et al. 2022, *arXiv preprint arXiv:2206.06641*
- Kupka, F., Piskunov, N., Ryabchikova, T. A., Stempels, H. C., & Weiss, W. W. 1999, *A&AS*, 138, 119
- Lehtinen, J., Jetsu, L., Hackman, T., Kajatkari, P., & Henry, G. W. 2016, *A&A*, 588, A38
- Llorente de Andrés, F., Chavero, C., de la Reza, R., Roca-Fàbrega, S., & Cifuentes, C. 2021, *A&A*, 654, A137
- López-Santiago, J., Montes, D., Fernández-Figueroa, M. J., & Ramsey, L. W. 2003, *A&A*, 411, 489
- López-Santiago, J., Montes, D., Gálvez-Ortiz, M. C., et al. 2010, *A&A*, 514, A97
- Maclaurin, D., Duvenaud, D., & Adams, R. P. 2015, in *ICML 2015 AutoML Workshop*, Vol. 238, 5

- Montes, D., Fernández-Figueroa, M. J., De Castro, E., et al. 2000, *A&AS*, 146, 103
- Montes, D., López-Santiago, J., Fernández-Figueroa, M. J., & Gálvez, M. C. 2001a, *A&A*, 379, 976
- Montes, D., López-Santiago, J., Fernández-Figueroa, M. J., & Ramsey, L. W. 2004, in *IAU Symposium*, Vol. 219, *Stars as Suns : Activity, Evolution and Planets*, ed. A. K. Dupree & A. O. Benz, 915
- Montes, D., López-Santiago, J., Gálvez, M. C., et al. 2001b, *MNRAS*, 328, 45
- Prša, A., Conroy, K. E., Horvat, M., et al. 2016, *ApJS*, 227, 29
- PyQT. 2012. <http://www.riverbankcomputing.com/static/Docs/PyQt4/html/index.html>
- Ramachandran, P., & Varoquaux, G. 2011, *Computing in Science & Engineering*, 13, 40
- Raskin, G., van Winckel, H., Hensberge, H., et al. 2011, *A&A*, 526, A69
- Ricker, G. R., Winn, J. N., Vanderspek, R., et al. 2015, *Journal of Astronomical Telescopes, Instruments, and Systems*, 1, 014003
- Schöfer, P. 2021, PhD thesis, Georg August University of Göttingen, Germany
- Strassmeier, K. G., & Rice, J. B. 2006, *A&A*, 460, 751
- Valenti, J. A., & Piskunov, N. 1996, *A&AS*, 118, 595
- Virtanen, P., Gommers, R., Oliphant, T. E., et al. 2020, *Nature Methods*, 17, 261
- Zhang, L.-Y., Pi, Q.-F., & Zhu, Z.-Z. 2015, *Research in Astronomy and Astrophysics*, 15, 252
- Zhu, C., Byrd, R. H., Lu, P., & Nocedal, J. 1997, *ACM Transactions on Mathematical Software*, 23, <https://doi.org/10.1145/279232.279236>

APPENDIX

A. TEST RESULTS

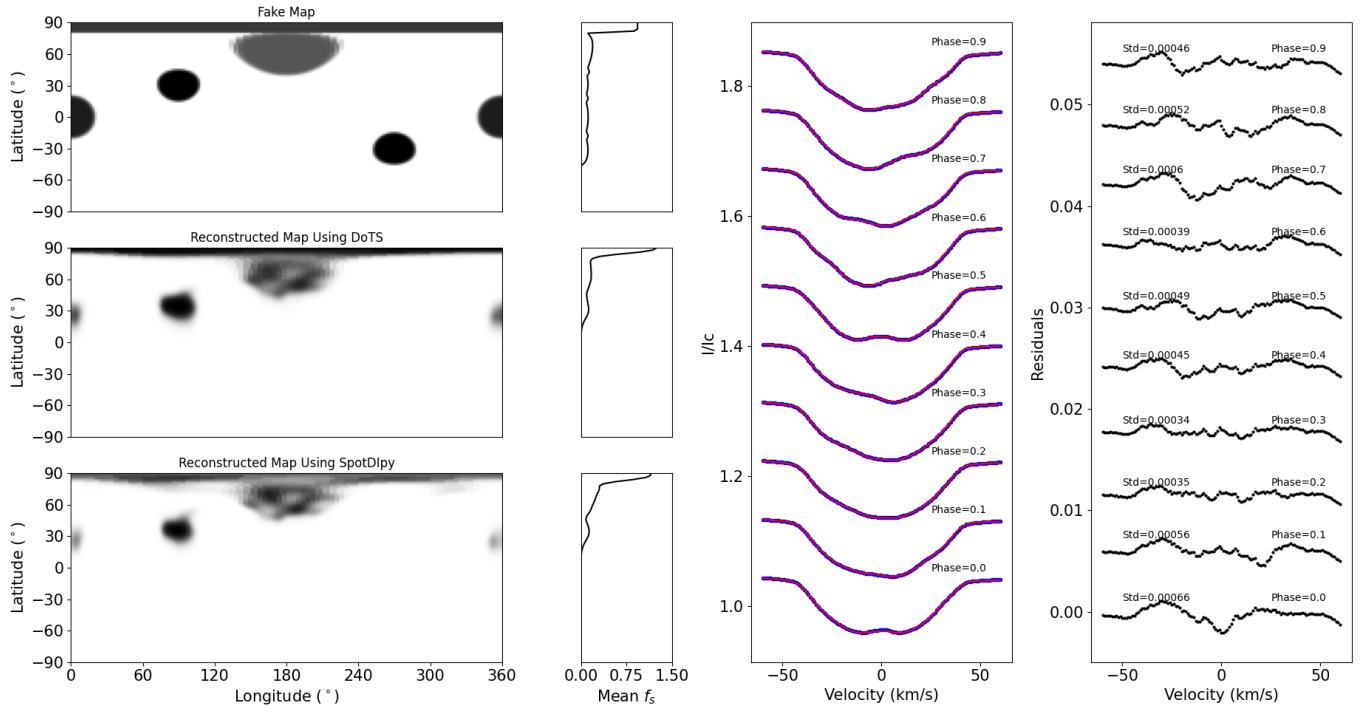


Figure 14. A comparison simulation of DoTS and SpotDIPy. In the first column, original spotted map (top) and reconstructed maps using DoTS (middle) and SpotDIPy (bottom), respectively. The third column shows latitudinal cross-section of the spots recovered. The third column shows the best fit models generated by DoTS (blue filled circles) and SpotDIPy (red solid lines). Differences between the best fit models with their standard deviations are shown in the fourth column. Phases corresponds to each best fits and residuals are indicated. Original spotted map and artificial synthetic line profiles with 500 S/N generated by DoTS under the 30° axial inclination.

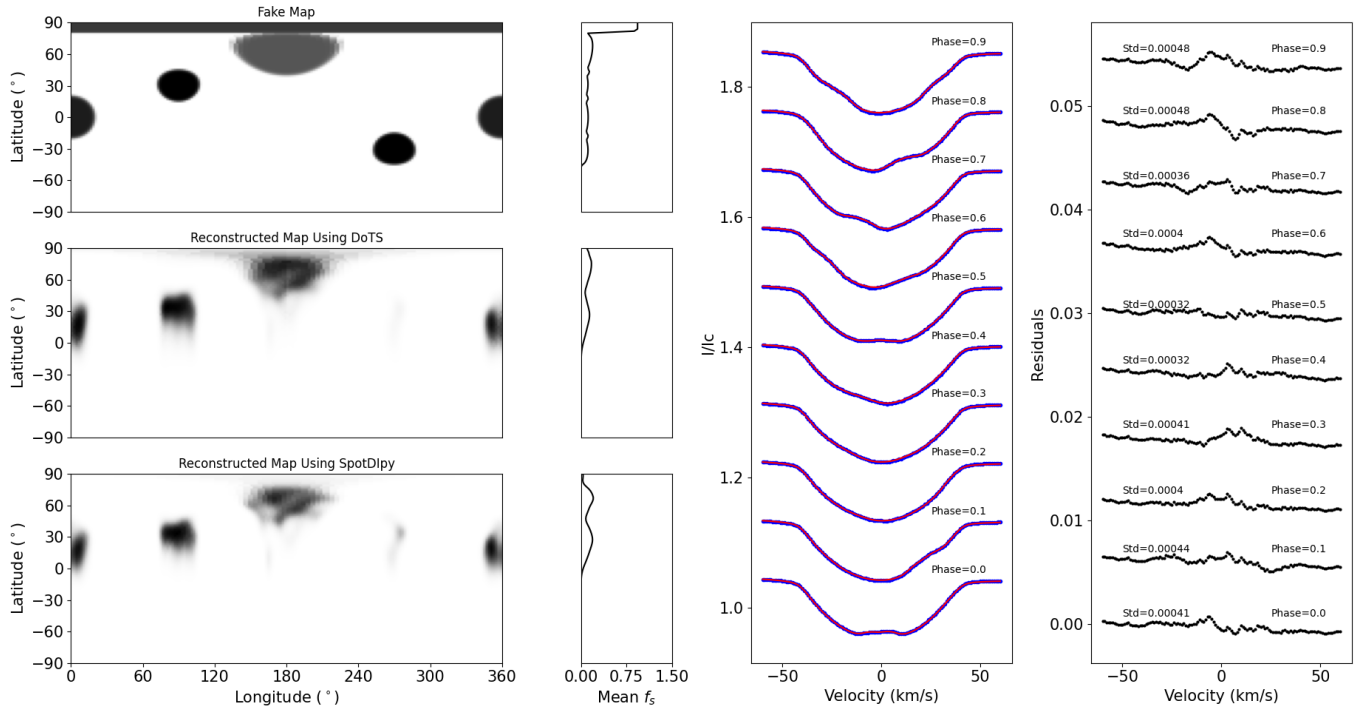


Figure 15. Same as Figure 14, but for 60° axial inclination.

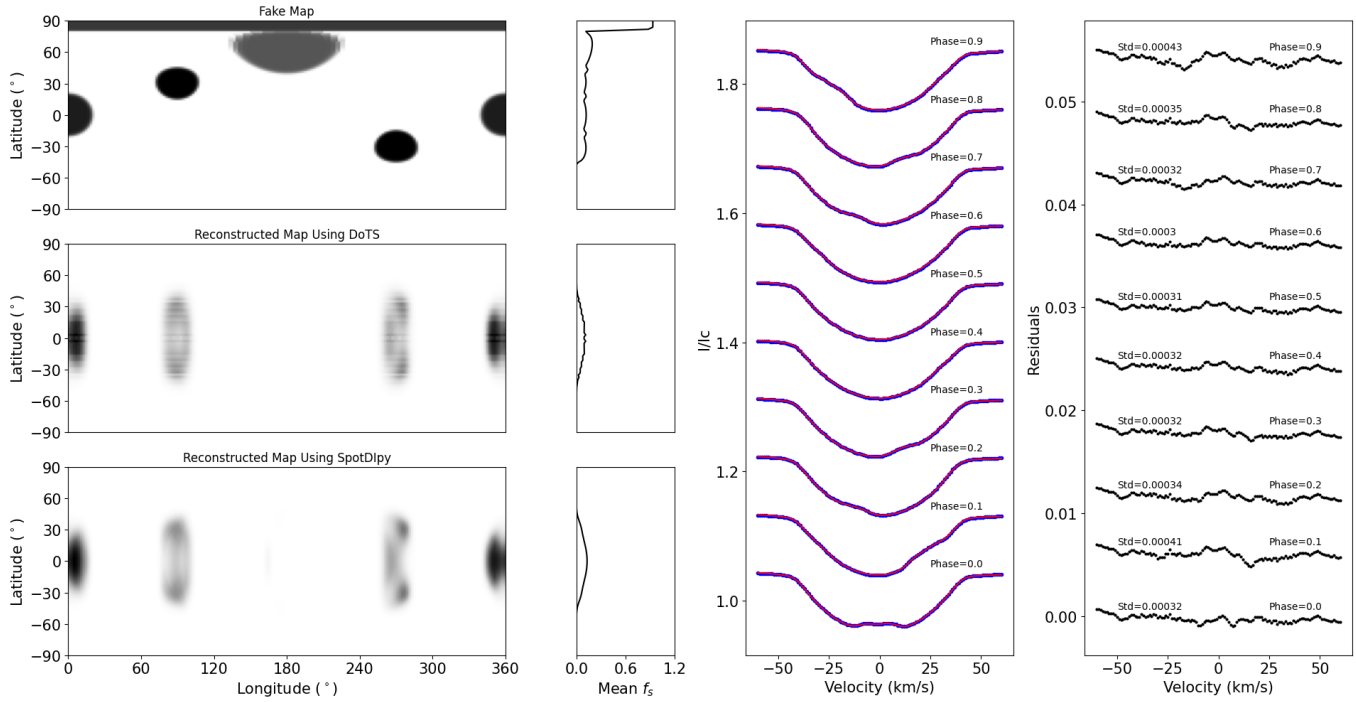


Figure 16. Same as Figure 14, but for 90° axial inclination.

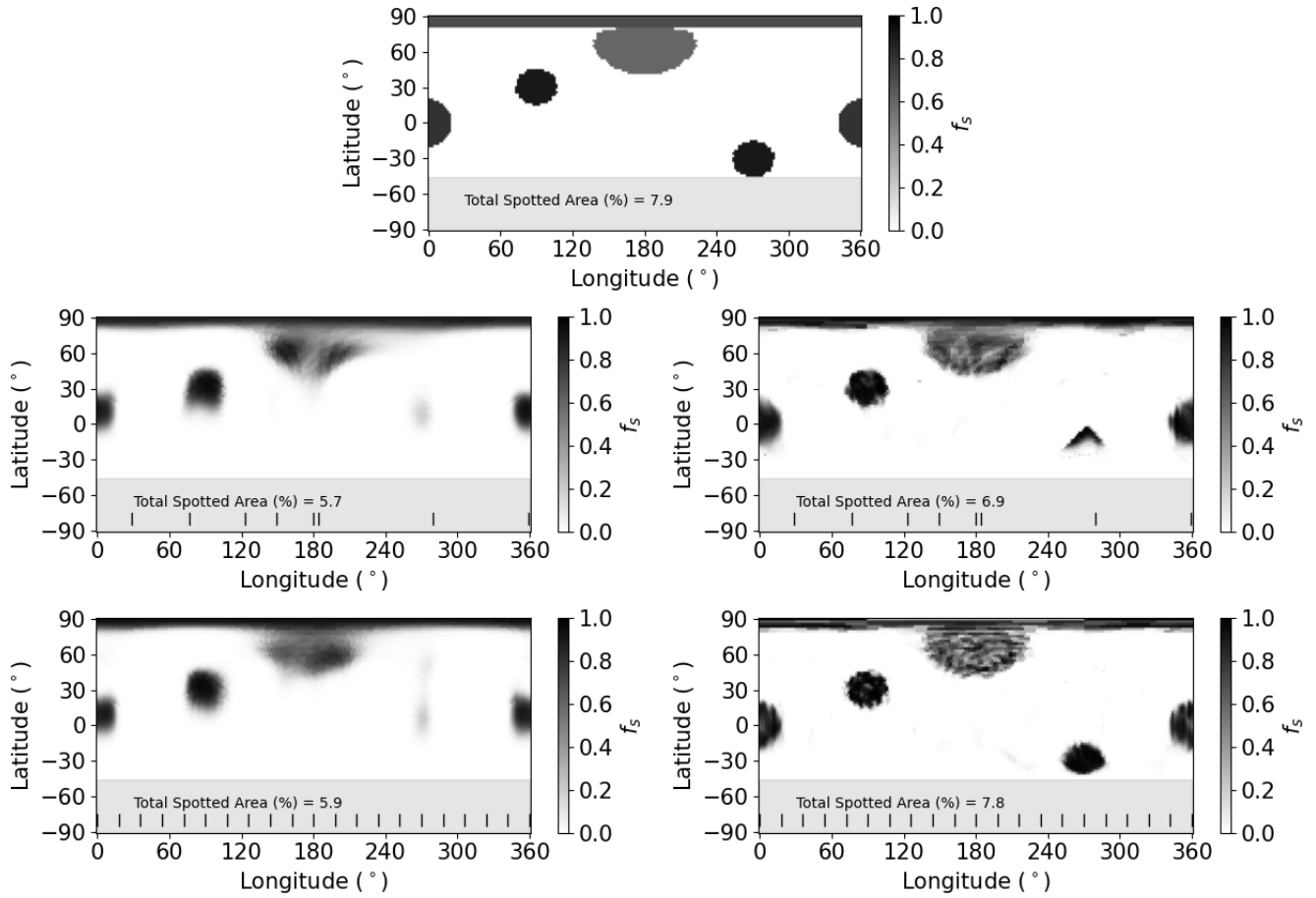


Figure 17. Test results for the effect of S/N and phase coverage on the reconstructed surface images. The top map is an artificial map containing spots placed at different latitudes and longitudes, and all artificial line profiles have been generated from this map. The middle left image was reconstructed using line profiles with the same phase coverage and S/N ratio as Set-1 data, while the lower left image used the same S/N ratio but with a 0.05 phase sampling interval. In the middle right image, we maintained the same phase coverage but with a significantly higher S/N ratio, while the lower right image combined a 0.05 phase sampling interval with a very high S/N ratio. The shaded region around the south pole of the projection indicates unseen region of the stellar surface.